

A Hybrid Tracked-Wheeled Multi-Directional Mobile Robot

Pinhas Ben-Tzvi

Robotics and Mechatronics Laboratory,
Departments of Mechanical Engineering,
Electrical and Computer Engineering,
Virginia Tech,
Blacksburg, VA 24061
e-mail: bentzvi@vt.edu

Wael Saab

Softwear Automation Inc.,
Atlanta, GA 30318
e-mail: waelaab@vt.edu

This paper presents the novel design and integration of a mobile robot with multi-directional mobility capabilities enabled via a hybrid combination of tracks and wheels. Tracked and wheeled locomotion modes are independent from one another, and are cascaded along two orthogonal axes to provide multi-directional mobility. An actuated mechanism toggles between these two modes for optimal mobility under different surface-traction conditions, and further adds an additional translational axis of mobility. That is, the robot can move in the longitudinal direction via the tracks on rugged terrain for high traction, in the lateral direction via the wheels on smooth terrain for high-speed locomotion, and along the vertical axis via the translational joint. Additionally, the robot is capable of yaw axis mobility using differential drives in both tracked and wheeled modes of operation. The paper presents design and analysis of the proposed robot along with a dynamic stabilization algorithm to prevent the robot from tipping over while carrying an external payload on inclined surfaces. Experimental results using an integrated prototype demonstrate multi-directional capabilities of the mobile platform and the dynamic stability algorithm to stabilize the robot while carrying various external payloads on inclined surfaces measuring up to 2.5 kg and 10 deg, respectively. [DOI: 10.1115/1.4043599]

Keywords: robot design, mechanism design, mobile robots, dynamics, control

1 Introduction

Modern field robotic technology is dominated by two main mobility systems: wheels (cylindrical, spherical, and omni-directional [1,2]) and caterpillar tracks. In field applications, the selection of a specific mobility system is contingent upon the terrain layout where the robot is expected to operate. Typically, wheel-based locomotion is favored for operations on smooth surfaces, as it provides fast maneuverability with minimal power consumption due to reduced friction with the ground. Alternatively, caterpillar tracks are more efficient on rugged terrains, including soft surfaces such as mud and sand, where the robot's load is distributed over a larger contact area with the ground. For field applications however, neither one of these two terrain layouts is constantly present. Instead, a more hybrid combination of both extremes dictates a topology where neither wheels nor tracks alone are efficient for optimal mobility on a real terrain. Such challenges, along with the expanding market for industrial, modular robotics, and human-assistive mobility technologies, has spurred research interest in a new generation of mobile robots capable of high levels of mobility in constrained environments and of adapting their form of locomotion in response to variations in the terrain layout. The most common of these are robots that combine wheels and tracks into a single platform, with broad variations in the integration of such transportation techniques. At the basic level of implementation, such robots consist of two timing belts wrapped around pulleys, with the possibility of manually attaching four off-centric wheels, one on each pulley hub, in order to switch from tracked to wheel-based mobility [3].

A more automated version of such an implementation employs a mechanism that changes the track shape or reconfigures linkages to expose driving wheels [4–7] with the possibility of integrating belt-driven front and back flippers [4] to further enable leg-like locomotion for military applications [8]. Other interesting variations of these solutions include articulated wheels that can be reconfigured into legs [9–11], and articulated tracks [12,13] that

can be reshaped into wheels; the latter being investigated as an advanced technology for mobility-assistive devices, such as wheelchairs [14].

A common denominator of the proposed solutions is the fact that the tracks are in constant motion, whether during tracked or wheeled mobility. In the latter, the tracks serve as a belt drive to transmit power from the motors to the wheel shafts. Furthermore, the versatility in mobility modes does not translate into a comparable versatility in mobility directions. In general, existing hybrid mobility robots are only capable of traditional longitudinal motion with differential steering, with no potential for lateral or omni-directional mobility [4]. This is a disadvantage, as these locomotion modes are shown to significantly improve the maneuverability of mobile robots in rugged and congested environments [15,16]. For a more detailed discussion the advantages and disadvantages of locomotion systems utilized in the field of mobile robots, the readers are encouraged to refer to Ref. [17].

The mobile robot proposed in this paper seeks to address these challenges via a novel design that integrates a wheeled and a tracked unit (TU) along two orthogonal axes of motion [17,18]. A prismatic mechanism toggles between the two mobility modes while maintaining operational symmetry of the platform to further enhance mobility during flip-over conditions. The future goal of this research will utilize the multi-directional and hybrid mobility of this robot to aid the reconfiguration procedure of modular robots on unstructured terrain, a concept that was thoroughly investigated in Ref. [17]. The benefits of multi-directional mobility for the proposed robot will enable precise translational (xyz) and rotational (yaw) misalignment between two modules while roll and pitch misalignments are intended to be compensated for via a high-misalignment tolerant coupling mechanism [19,20]. For simulated case scenarios demonstrating the benefits of the proposed robot, the readers are encouraged to refer to Ref. [21].

The design details of the proposed robot are presented in this paper, along with analyses and development of a dynamic stabilization algorithm. An experimental prototype is further integrated to validate the algorithmic component of dynamic stability. The experimental results demonstrate that the proposed mechatronic system represents a valuable hybrid multi-directional mobility platform that can be used for industrial, modular, and mobility-assistive robotic applications.

Contributed by the Mechanisms and Robotics Committee of ASME for publication in the JOURNAL OF MECHANISMS AND ROBOTICS. Manuscript received May 24, 2018; final manuscript received April 11, 2019; published online May 17, 2019. Assoc. Editor: Robert J. Wood.

2 Design Overview

The mechanical design architecture of the hybrid, tracked-wheeled, multi-directional mobile robot is presented in this section to provide the reader with the necessary design details in terms of the overall mechanical design structure. This section also presents the related electrical hardware architecture that supports the mechanical design and the various mobility configurations. Further details of the proposed robot design are available in Refs. [17,18].

2.1 Mechanical Design. The proposed robot, shown in Fig. 1(a), consists of a vertical translation mechanism (VTM) cascaded between two independently actuated tracked units to maintain the overall symmetry of the platform. A prismatic joint within the VTM connects two independently actuated wheeled units in the middle to enable translation of the TUs along the Z-axis.

The axes of motion of the tracked and wheeled units are orthogonal to one another to enable longitudinal X-axis and lateral Y-axis mobility, respectively; in addition to vertical translation along the Z-axis shown in Figs. 1(b) and 1(c). The transition from one locomotion mode to another is enabled by the VTM prismatic joint, where the wheeled units are lifted above the ground for tracked longitudinal mobility Fig. 1(b). Alternatively, for lateral mobility, the wheeled units are deployed down along the prismatic joint to push against the ground and raise the tracked units Fig. 1(c). Since both the wheeled and tracked units are independently driven, the robot can produce differential drive turning about the yaw Z-axis during both modes of locomotion.

The hull of the tracked unit shown in Fig. 2 consists of two parallel side plates that house two pulley sets: one active pulley driven by a geared motor and one passive pulley whose rotation is initiated by external tracks, as depicted in the detailed assembly shown in Fig. 1. The tracks are further supported by two passive rollers in the middle section of the tracked unit hull to protect and isolate internal components from damage. Each tracked unit further carries a motor driver and a battery pack, which are together connected in series to supply power to the power control board placed in the VTM.

The wheeled unit (WU), shown in Fig. 3, consists of a DC motor and four wheels, each located at the corners of the frame (an opposing metal frame that supports the shafts of the motor and wheels

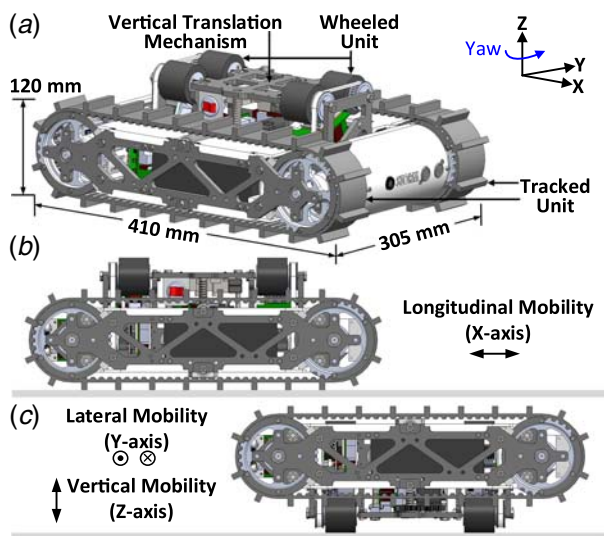


Fig. 1 CAD model of the proposed hybrid mobility robot: (a) the isometric view of the robot, (b) the tracked locomotion mode in the longitudinal direction, and (c) the wheeled locomotion mode in the lateral direction

has been hidden to better illustrate its internal components). Improvements from the preliminary design concept presented in Ref. [17] include: (1) replacement of a servo motor with a DC motor and motor driver assembly for high-speed locomotion and speed control using hall effect sensor feedback and (2) replacement of power transmission using a spur gear with a timing belt system that drives all four wheels to provide better rotary power transfer to the ground.

The VTM, shown in Fig. 4, represents the prismatic joint along which the relative displacement between the wheeled and tracked units occurs. The wheel units are connected to the sides of the VTM at the attachment points. The prismatic joint is driven by a geared DC motor (powered by the tracked units' batteries) through 1:1 spur gear assembly that drives a lead screw mechanism. The lead screw nut is directly attached to the tracked unit to create relative displacement upon rotation of the lead screw; however, this attachment is not shown in Fig. 4. The position of the VTM relative to the tracked unit is monitored using a linear

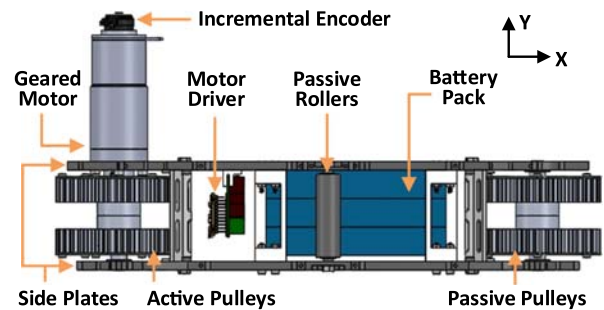


Fig. 2 CAD model of the tracked unit with the tracks removed to show the internal components

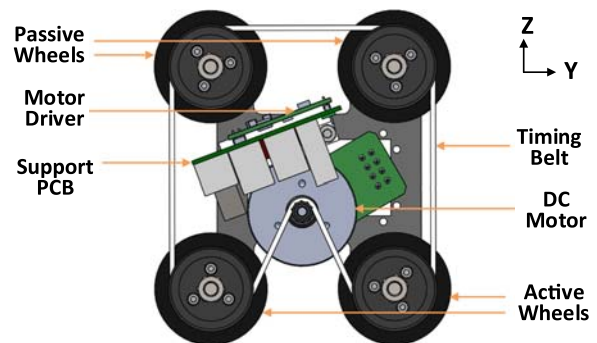


Fig. 3 CAD model of the WU

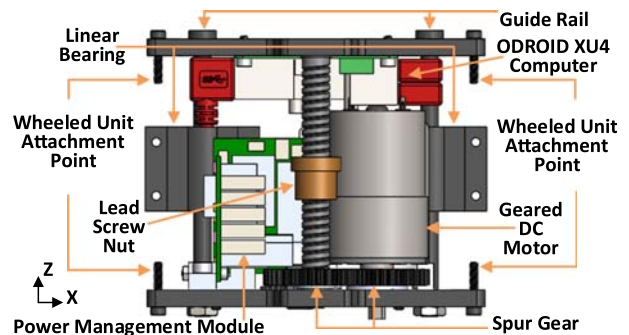


Fig. 4 CAD model of the VTM

potentiometer. The vertical translational of the VTM is further guided by a pair of linear guide rails and linear bearings that are connected to the inside metal plate of the tracked units for additional structural support. The VTM also houses electronics for motor control and power management.

2.2 Electrical Hardware Architecture. The electrical hardware architecture, depicted in Fig. 5, provides onboard wireless control interfaces between the robot and operator control unit (OCU). The robot is powered by a 28.8 V high discharge battery pack (12 A maximum). The power management module in the VTM distributes a stable 5 V and 14 V power source to the electrical components.

The electrical hardware shown in Fig. 5 is divided into two subsystems: sensing and actuation. In the sensing subsystem, a Teensy 3.2 Microcontroller is used to control sensing and communication. Ultrasonic distance sensors and 5MP USB cameras are mounted on the front and rear of the robot to provide objects' distance information and imagery readings, respectively. The two wheel motors powering the WU and TU are synchronized using a proportional integral differential (PID) controller to ensure straightforward and backward motion and efficient turning with minimal wheel slippage [22]. The power to the motor drivers and the VTM servo is controlled by the microcontroller through a solid-state "high side" switch. A 9-axis inertial measurement unit (IMU) is used to measure and transmit acceleration and angular rates of the robot. The wireless communication between the robot and the OCU is established using both a Wi-Fi module and an Xbee RF that is connected to the Teensy MCU for transferring motion control commands. The robot also hosts an ODRROID XU4 onboard computer for high-level computation.

3 Dynamic Stability Control

In this section, the stability of the hybrid mobility robot during wheeled locomotion is explored. In this mobility mode, the tracked units are cantilevered above the ground, which narrows the width of the effective wheelbase. This makes the robot prone to rollover instability as a result of inertial dynamics acting on the tracked units during acceleration and deceleration, and thus requires a special controller to saturate these inertial effects and smooth the trajectory to avoid tip-over. This controller is of particular interest in the presence of an external payload, such as during object transportation or in applications where the hybrid robot is employed as a mobility mechanism or pick/place robot in industrial settings.

3.1 Related Work. In dynamic systems, the inertial linear and rotational dynamics act against the intended motion by shifting the load counter to the direction of acceleration. This behavior is well recognized in wheeled vehicular technology [23,24] where the transfer of load forces causes some of the wheels to gradually lose contact with the ground [25], causing loss of traction [26,27] or tip-over instability in vehicles [28] and mobile robotics.

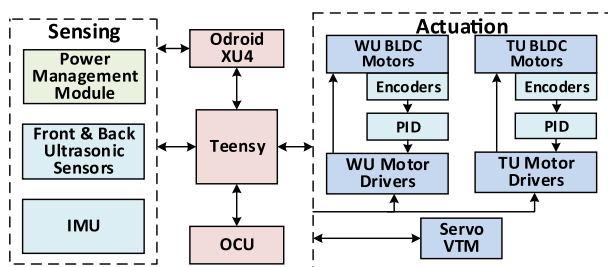


Fig. 5 Schematic diagram depicting mechatronic implementation sensing and actuation

Maintaining dynamic stability becomes of critical importance for mobile robots that undergo fast maneuvers, climb inclined terrains, or manipulate heavy objects. Messuri and Klein proposed the use an "Energy Stability Margin" that computes the minimum potential energy required to knock over a robot over about its edges [29]. This work was later extended by Ghasempoor and Sepeheri to include dynamic inertial and external loads [30]; however, the approach was simulation based to provide operators with knowledge of unsafe configurations during manipulation operations. For practical implementation onboard a wheeled robot, a modified velocity-based energy margin was proposed that computed energy required for tipping over using the rotational velocity feedback [31]. This approach did successfully indicate instances when the mobile robot would lose stability, but was not used for online control to prevent tipping over motions. McGhee and Frank proposed the margin of static stability [32], the shortest horizontal distance between the center of mass (COM) and the supporting edge projected onto a horizontal plane which was later extended by Song and Waldron for the analysis on inclined terrains [33]. Both of these static stability margins were used to generate stable quasistatic walking gaits that were implemented on physical legged robotic systems. To extend this concept to dynamic systems, Sugano et al. demonstrated the first implementation of the zero-moment-point (ZMP) criteria for a mobile manipulation robot [34], a criteria initially used for designing stable dynamic gaits for anthropomorphic robots [35]. However, if the ZMP is calculated in a way presented in Ref. [34], the mass moment of inertia of rigid bodies will be neglected and provides only an approximation of stability on uneven/inclined terrains. In a later work, the mass moment of inertia was added to the original ZMP formulation for real-time stability compensation on a simulated mobile manipulation robot [36]. Papadopoulos and Rey presented another stability criteria called the "Force-Angle Margin" that measures the minimum angle between the resultant force at the base and tip-over axis subjected to a low velocity tip-over assumption that was demonstrated using a vehicle simulation [37]. Physical implementation of this method was demonstrated on a Packbot mobile manipulation platform [38] that maintains stability during static operations that takes into consideration gravitational and steady state forces acting on the robot.

In review, the majority of related work regarding stability of indicators and control of mobile robots was demonstrated in simulation environments. Practical implementation has been demonstrated for online static stability control [38], and indicating moments of dynamic instability [31].

To analyze the inertial dynamics of the proposed hybrid mobility robot, please refer to the nomenclature with reference to Fig. 6.

3.2 Stability Dynamic Formulation. For the physical implementation of the dynamic stability formulation on the proposed robotic system, we propose an algorithm which is time efficient

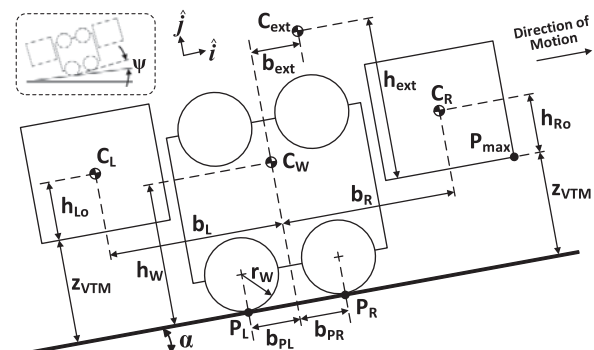


Fig. 6 Schematic of the hybrid mobility robot during wheeled locomotion

and requires minimal sensory feedback as will be discussed in more detail in this section. Since the aspect ratio of the wheel contact points with the ground is equivalent to 0.375, the robot is prone to dynamic instability along the direction of motion in the ij -plane, depicted in Fig. 6, which corresponds to the narrowest wheelbase. This reasoning, coupled with the robot's ability to accurately produce straight line motions due to motor velocity PID synchronization (Sec. 2.2), justifies the analysis of planar stability along the direction of motion.

This algorithm seeks to ensure that the optimal rate of change in the robot's velocity is at all time satisfying the conditions

$$\eta_{P_L}^a \leq 0 \quad \text{and} \quad \eta_{P_R}^d \geq 0 \quad (1)$$

where $\eta_{P_L}^a$ and $\eta_{P_R}^d$ define the combined moment of all external forces acting on the robot's pivot axis about the point P_L during acceleration and P_R during deceleration phases, respectively. The equality constraints in Eq. (1) resemble the scenario when the ZMP is located at the supporting edge (no stability margin). The inequalities ensure the sufficient loading to maintain ground contact with both wheels while satisfying the trivial constraint of static stability, where the projected COM falls between points P_L and P_R [32], which for the proposed robotic system is satisfied due to its symmetric construction and mass distribution. Satisfying these conditions ensures no pitching motion of the robot that may cause instability during locomotion.

During acceleration in the direction of motion (Fig. 6), $\eta_{P_L}^a$ can be further expanded to reflect the contribution of three different components as

$$\eta_{P_L}^a = \eta_{grav}^a + \eta_{lin}^a + \eta_{ang}^a \quad (2)$$

where the superscript a denotes acceleration, η_{grav}^a the combined moment of gravitational forces, and $\eta_{lin}^a, \eta_{ang}^a$ the moments resulting from linear and angular inertial dynamics, respectively. By further expanding these components, the sum of gravitational and linear inertial moments can be written as

$$\eta_{grav}^a + \eta_{lin}^a = \left\{ \begin{array}{l} M_L(P_L C_L) + M_R(P_L C_R) + \\ M_W(P_L C_W) + M_{ext}(P_L C_{ext}) \end{array} \right\} \times (g + a_{inert}) \quad (3)$$

where, with reference to Fig. 6, the dimensional vectors in Eq. (3) can be expanded as

$$\begin{aligned} P_L C_L &= -(b_L - b_{P_L})\hat{i} + (h_{L_0} + z_{VTM})\hat{j} \\ P_L C_R &= (b_R + b_{P_L})\hat{i} + (h_{R_0} + z_{VTM})\hat{j} \\ P_L C_W &= b_{P_L}\hat{i} + h_W\hat{j} \\ P_L C_{ext} &= (b_{P_L} + b_{ext})\hat{i} + (h_{ext} + z_{VTM})\hat{j} \end{aligned} \quad (4)$$

and the gravitational and inertial acceleration vectors as

$$g = -|g| \sin(\alpha)\hat{i} - |g| \cos(\alpha)\hat{j} \quad (5)$$

and

$$a_{inert} = -a_x\hat{i} \quad (6)$$

where $|g|$ is the magnitude of the gravitational force. In Eq. (6), a_x defines the acceleration component along the direction of motion (Fig. 6).

Similarly, one can expand the moment component of the inertial angular acceleration as

$$\eta_{ang}^a = v(\psi)J_{P_L}\ddot{\psi} \quad (7)$$

where J_{P_L} defines the combined polar moment of inertia about the pivot and $v(\psi)$ a tuning parameter that controls the amount of inertial pitch inclination allowed in the system. The value of this parameter is a compromise choice between the speed of the robot and the maximum allowed pitch oscillation based on a good priori knowledge of the robot's operating conditions. For instance, a positive value of $v(\psi)$ allows a proportional amount of oscillations in the system, but enables the robot to accelerate (or decelerate) at a faster rate. Conversely, a negative value will reduce the robots' ability to accelerate (or decelerate); therefore, resulting in slower motions. For unknown or variable terrain and payload conditions, this parameter would preferably be set to zero which can be updated in real-time based on the observed performance of the robot. This parameter was empirically tuned in a series of experiments to a value of -1.4 that resulted in fast and stable motions with minimal pitching motions during wheeled locomotion. Section 4.2 presents a further refinement to this tuned parameter based on experimental results. In Eq. (7), $\ddot{\psi}$ further defines the rate of pitch angular acceleration which can be expressed as

$$\ddot{\psi} = -a_x/\rho_{P_L} \quad (8)$$

where ρ_{P_L} represents the radius of gyration of the combined polar inertia relative to the pivot. Note that in Eq. (8), pitch rotation is assumed to be negligible due to the design of this controller satisfying Eq. (1) and a no-slip condition was considered as viable for dynamic instability as will be further discussed subsequently.

Based on these derivations, the resolution of the stability condition satisfying Eq. (1) generates a closed-form expression for the upper limit on robot acceleration as

$$a_{max}^a \leq g \frac{\left(\begin{array}{l} \cos \alpha [(b_{ext}M_{ext} - b_L M_L + b_R M_R + b_{PL}(M_{ext} + M_L + M_R + M_W))] \\ - \sin \alpha [h_{ext}M_{ext} + h_{L_0}M_L + h_{R_0}M_R + h_W M_W + (M_{ext} + M_R + M_L)z_{VTM}] \end{array} \right)}{\left(\begin{array}{l} M_L(h_{L_0} + z_{VTM}) + M_R(h_{R_0} + z_{VTM}) \\ + M_W h_W + M_{ext}(h_{ext} + z_{VTM}) - v(\psi)J_{P_L}/\rho_{P_L} \end{array} \right)} \quad (9)$$

which represents a direct function of z_{VTM} , α , and ψ . In an identical scheme, one can derive a closed-form expression for the lower limit on robot deceleration as

$$a_{max}^d \geq -g \frac{\left(\begin{array}{l} \cos \alpha [-b_{ext}M_{ext} + b_L M_L - b_R M_R + b_{PR}(M_{ext} + M_R + M_W + M_L)] \\ + \sin \alpha [h_{ext}M_{ext} + h_{L_0}M_L + h_{R_0}M_R + M_W h_W + (M_{ext} + M_R + M_L)z_{VTM}] \end{array} \right)}{\left(\begin{array}{l} M_L(h_{L_0} + z_{VTM}) + M_R(h_{R_0} + z_{VTM}) \\ + M_W h_W + M_{ext}(h_{ext} + z_{VTM}) - v(\psi)J_{P_L}/\rho_{P_L} \end{array} \right)} \quad (10)$$

where

$$\begin{aligned} P_R C_L &= -(b_L + b_{P_R})\hat{i} + (h_{L_0} + z_{VTM})\hat{j} \\ P_R C_R &= (b_R - b_{P_R})\hat{i} + (h_{R_0} + z_{VTM})\hat{j} \\ P_R C_W &= -b_{P_R}\hat{i} + h_W\hat{j} \\ P_R C_{ext} &= -(b_{P_R} - b_{ext})\hat{i} + (h_{ext} + z_{VTM})\hat{j} \end{aligned} \quad (11)$$

and

$$a_{inert} = a_x \hat{i} \quad (12)$$

LEMMA. *In dynamic stability control of mobile robotics subject to eccentric loading, a reduction in surface traction resulting in increased longitudinal slip velocity ξ_L ($\xi_L > 0$) plays in favor of the robot's balance.*

Proof. Consider a mobile robot with a linear velocity component v_{Rob}^{eff} in the direction of motion (Fig. 6) defined by

$$v_{Rob}^{eff} = R_W \omega - \xi_L \quad (13)$$

where ω denotes the wheels' angular velocity (rad/s) and R_W the wheels' radius. The first-order time derivative of Eq. (13) generates an expression for the effective linear acceleration of the robot as $a_{Rob}^{eff} = R_W \dot{\omega} - \dot{\xi}_L$, with $a_{Rob}^{eff} = dv_{Rob}^{eff}/dt$. However, if a_{max}^a is calculated according to Eq. (9), which assumes a no-slip condition, then $a_{max}^a = R_W \dot{\omega}$ and represents the maximum allowable acceleration prior to the onset of destabilizing oscillations. This means that the effective robot acceleration in the direction of motion in the presence of longitudinal slip can be written as

$$a_{Rob}^{eff} = a_{max}^a - \dot{\xi}_L \leq a_{max}^a \quad (14)$$

which is less, or at best, equals to a_{max}^a in Eq. (9). This infers that in the presence of slip, the robot's tendency to exhibit rollover oscillations will be diminished if the rate of change in velocity is controlled by a_{max}^a in Eq. (9).

A similar proof can be obtained for the deceleration case. ■

3.3 Control Algorithm. In the proposed stability algorithm, ω_0 is defined as the motors' angular velocity at $t = t_0$ and ω_{req} as the required angular velocity at $t = t_0 + \Delta t$. ω_0 is measured from the motors' encoders, while ω_{req} is a system input initiated either by an operator or by a higher level controller. Based on these two inputs, a second-order approximation of the required angular acceleration can be calculated in real-time. That is, for $f(t) = \omega(t)$ with $f(t_0) = \omega_0$ and $f(t_0 + \Delta t) = \omega_{req}$, a second-order Taylor series expansion around t_0 can be rearranged into the differential form

$$\dot{\omega}_{req} = f'(t_0) + \frac{1}{2} f''(t_0) \Delta t \quad (15)$$

where, by definition, we set $\dot{\omega}_{req} = (f(t_0 + \Delta t) - f(t_0))/\Delta t$ in Eq. (15) as the required motor angular acceleration.

Using a central difference scheme, the first- and second-order derivatives in Eq. (15) can be further approximated as

$$f'(t_0) = \frac{\omega(t_0 + \Delta t) - \omega(t_0)}{\Delta t} = \frac{\omega_{req} - \omega_0}{\Delta t} \quad (16)$$

and

$$f''(t_0) = \frac{\omega(t_0 + \Delta t) - 2\omega(t_0) + \omega(t_0 - \Delta t)}{\Delta t^2} \quad (17)$$

In Eq. (17), $\omega(t_0 - \Delta t) = \omega_0$ since by definition, we considered a change in angular velocity between time t_0 and $t_0 + \Delta t$. The substitution of Eqs. (16) and (17) back into Eq. (15) yields the second-order linear approximation of the required motor angular acceleration as

$$\dot{\omega}_{req} = \frac{3}{2} \left(\frac{\omega_{req} - \omega_0}{\Delta t} \right) \quad (18)$$

which can be very efficiently be calculated in real-time. While $\dot{\omega}_{req}$ defines the motor's angular acceleration rather than the robot's linear acceleration, a relationship between the latter and $\dot{\omega}_{req}$ can be established by taking advantage of the valid no-slip condition. This expression can be written as

$$\begin{aligned} a_{Rob}^{req} &= \lambda \dot{\omega}_{req} \\ \lambda &= \frac{R_W}{K_{gear}} \end{aligned} \quad (19)$$

where $K_{gear} > 1$ defines the combined ratio of gear transmission between the motor and the wheels. Based on these derivations, and with an a priori knowledge of pertinent mechanical (K_{gear} , R_W , etc.) and dynamic parameters (masses, inertias, $v(\psi)$, dimensional vectors, etc.), the algorithm given in Table 1 can be established.

For this algorithm, a linear discrete interpolation between ω_0 and ω_{req} was chosen, with a sampling period T to control the motor angular velocity ω_m , as follows:

$$\omega_m(k) = \text{sgn}(\dot{\omega}_{req}) \dot{\omega}_{req} (t_0 + kT) + \omega_0 \quad (20)$$

where $k = \Delta t_{cor}/T$, with Δt_{cor} defining the corrected time span between ω_0 and ω_{req} , and sgn the sign function. Note that other interpolations for $\omega_m(k)$ are also possible, such as quadratic, cubic, or quintic, among others.

3.4 Dynamic Stability Controller Simulation. The dynamic stability algorithm was simulated for the robot in the wheeled

Table 1 Stability control algorithm

1.	while (1)
2.	Inquire sensor feedback ω_0 (from motor encoders), a (from onboard IMU), ω_{req} (from higher level controller or operator (joystick))
3.	Inquire Δt either from a higher level controller, or by monitoring the elapsed time between operator input commands
4.	Inquire z_{VTM} from potentiometer, and $\dot{\omega}_{req}$ and a_{Rob}^{eff} from Eqs. (18) and (19), respectively
5.	If $\dot{\omega}_{req} > 0$ Calculate a_{max}^a based on Eq. (9), and set count = 1 (where count is a dummy variable) else If $\dot{\omega}_{req} < 0$ Calculate a_{max}^d based on (10) and set count = 2 else continue end (case structure @5)
6.	If count = 1, i.e., <i>acceleration</i> If $a_{Rob}^{eff} \leq a_{max}^a$ continue (no correction required) else (correct the slope) Calculate $\dot{\omega}_{cor} = a_{max}^a / \lambda$ (corrected angular acceleration) Calculate $\Delta t_{cot} = \frac{3}{2} \left(\frac{\omega_{req} - \omega_0}{\dot{\omega}_{cor}} \right)$ and increase motor speed according to: $\omega_m(k) = \dot{\omega}_{req} (t_0 + kT) + \omega_0^a$ end end (case structure @ 6)
7.	If count = 2, i.e., <i>deceleration</i> If $ a_{Rob}^{eff} \leq a_{max}^d $ continue (no correction required) else (correct the slope) Calculate $\dot{\omega}_{cor} = a_{max}^d / \lambda$ (corrected angular deceleration) Calculate $\Delta t_{cot} = -\frac{3}{2} \left(\frac{\omega_{req} - \omega_0}{\dot{\omega}_{cor}} \right)$ and decrease motor speed according to: $\omega_m(k) = -\dot{\omega}_{req} (t_0 + kT) + \omega_0^a$ end end (case structure @ 7) (<i>reset count to zero</i>) end (while loop @ 1)

^aRefer to Eq. (20).

locomotion mode with estimated mass and geometric properties obtained from computer-aided design software, shown in Table 2. Figure 7 shows a plot of maximum allowable acceleration, evaluated using Eq. (9) for various ground inclination angles (α) and external payloads (M_{ext}) attached to the robot at a fixed elevated height of $h_{ext} = 750$ mm while considering updated values of $J_{PL,R}$ and $\rho_{PL,R}$ to account for the added inertia using the parallel axis theorem. It can be observed from this plot that the maximum allowable acceleration reduces exponentially with an increase of M_{ext} and α . The results of this simulation were used to compute the maximum allowable accelerations of the robot in order to experimentally evaluate the performance of the dynamic stability control algorithm.

4 Prototype Integration and Experimental Results

This section discusses the integration of the hybrid, tracked-wheeled, multi-directional mobile robot prototype (Sec. 4.1), along with experimental results to demonstrate its locomotion capabilities, verify the dynamic stability control algorithm while carrying an external payload (Sec. 4.2), and demonstrate the benefits of multi-directional mobility (Sec. 4.3). For videos of these experiments, the readers are encouraged to refer to Ref. [21].

4.1 Prototype Integration. Structural components of the prototype, shown in Fig. 8, were manufactured from aluminum and stainless steel. In addition, polymer mud/dust guards were installed to protect internal components from debris. The robot weighs 9 kg and can reach a maximum speed of 3.55 m/s and 2.65 m/s on flat terrain during wheeled and tracked locomotion, respectively. With a zero velocity initial condition, the robot can climb inclinations angles of up to 18 deg –48 deg with wheeled and tracked locomotion, respectively. Figure 8 demonstrates the advantages of hybrid locomotion where the robot can perform high-speed locomotion using wheeled locomotion on a relatively uniform surface such as asphalt, Fig. 8(a), then switching to the high traction tracked locomotion mode for a rugged dirt and rock terrain, Fig. 8(b).

Table 2 Physical parameters of the robot

Parameter	Value	Parameter	Value
b_{ext}	0 mm	z_{vm}	40 mm
h_{Lo}, h_{Ro}	60 mm	M_W	2.63 kg
g	9.8 m/s ²	M_L, M_R	3.185 kg
b_{PL}, b_{PR}	36.2 mm	h_W	90.1 mm
b_L, b_R	112.5 mm	$J_{PL,R}$ (no load)	0.1549 kg m ²
$\rho_{PL,R}$ (no load)	94.1 mm	R_W	22 mm
K_{gear}	15	$v(\psi)$	-1.4

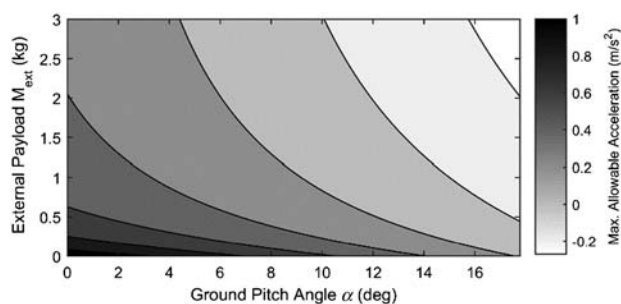


Fig. 7 Computed simulation results of maximum allowable acceleration as a function of ground pitch angle and external payload

4.2 Dynamic Stability Control. A series of experiments were performed to test the dynamic stability control algorithm's ability to prevent the robot from tipping over during wheeled locomotion. Three case scenarios were conducted where an external payload of $M_{ext} = \{0, 1, 2.5\}$ kg was attached to the robot at a constant elevated height $h_{ext} = 750$ mm, with no longitudinal offset $b_{ext} = 0$ cm. The robot was then commanded to move forward in a straight line with a 2 second acceleration phase, then a 2 second deceleration phase utilizing open loop velocity control, then compared with the results of the robot performing the same experiment with the dynamic stability algorithm implemented. Each case scenario was evaluated with ten trials to maintain consistency. Measured results of robot acceleration and wheel speed were then averaged and standard deviation was computed.

For the no load case scenario $M_{ext} = 0$ kg on flat terrain, shown in Fig. 9, it is interesting to note that for both controlled and uncontrolled modes, during the acceleration phase, the robot acceleration (Fig. 9(a)) is relatively equivalent (except for a control action observed at 0.4 s) since the system maintains an acceleration within the maximum allowable acceleration region of ± 1.3 m/s² (Fig. 7). However in the controlled mode, at 0.4 s the algorithm reduced the robot's acceleration as the measured value exceeded the allowable magnitude, hence an acceleration reduction is observed coupled with a decrease in wheel angular velocity in comparison to the uncontrolled mode (Fig. 9(b)). In the deceleration region, an approximate 0.3 s time delay after the 2 s mark is observed where the robot still experiences a positive acceleration due to the electro-mechanical inertial properties of the system and time response of the controller. In the controlled mode, the robot experiences less deceleration extended over a longer time span that results in a more gradual decrease of wheel velocity and a

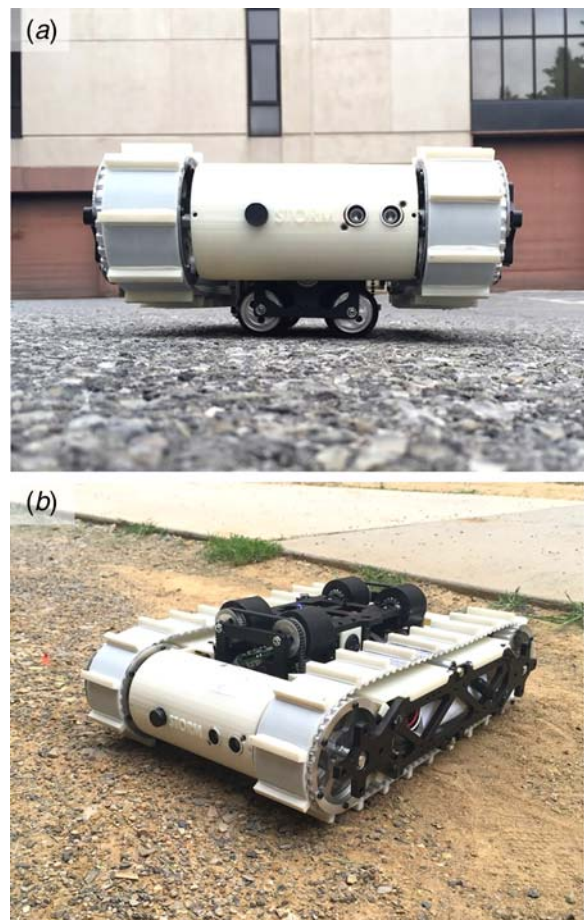


Fig. 8 Integrated prototype: (a) wheeled and (b) tracked locomotion mode

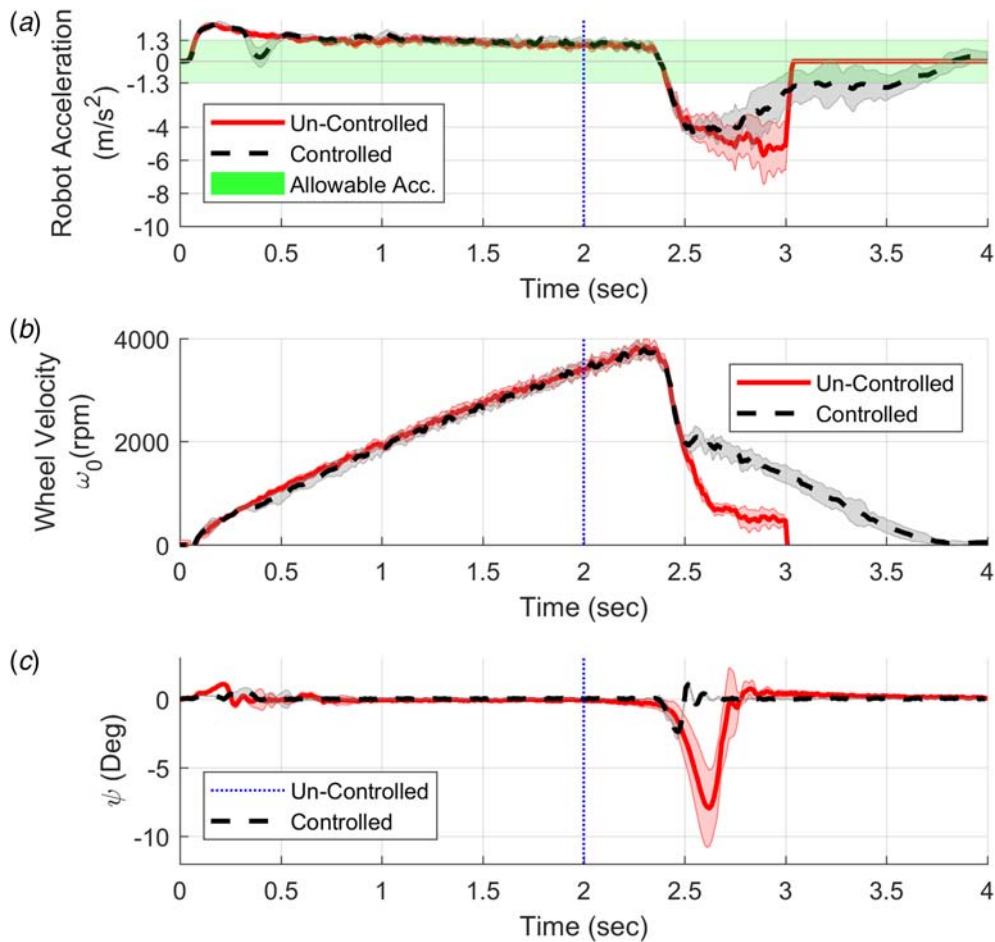


Fig. 9 Experimental results of a no payload $M_{ext} = 0$ kg case scenario: (a) robot acceleration, (b) wheel velocity, and (c) robot pitch angle ψ

stable stop of the robot. In the uncontrolled mode, the effects of the high deceleration and sudden drop of wheel velocity caused the robot to tip-over. The effects of the controller are most visible in the measurements of the robot pitch angle (Fig. 9(c)) during the deceleration phase. Without control the robot reaches an average maximum pitch angle equivalent to -7.9 deg; however pitching motion is reduced to a maximum value of -2.3 deg where the front wheels were observed to lift slightly off the ground. In such scenarios, the incremental adjustments to the tuning parameter, v (ψ), may be performed to reduce its value that was initially set to -1.4 (Table 2). Incremental reductions of this parameter will reduce the amount of acceleration or deceleration the robot can produce during locomotion which will result in less pitch angular oscillations during locomotion.

For the $M_{ext} = 1$ kg case scenario on flat terrain, shown in Fig. 10, during the acceleration phase the robot exceeds the maximum allowable acceleration of ± 0.6 m/s² (Fig. 7). Due to the additional mass and reduced allowable acceleration range, more control action is observed in attempts to reduce the robot's acceleration (Fig. 10(a)) at time instances {0.2, 0.6, 1} s that also reduced wheel velocity (Fig. 10(b)). In the deceleration region of the uncontrolled mode, a sharp decrease in wheel velocity results in a large robot deceleration reaching up to an average value of -7.2 m/s² that caused the robot to lose stability and tip-over reaching a maximum pitch angle equivalent to 10.5 deg (Fig. 10(c)). In the controlled mode, the robot acceleration and deceleration are maintained relatively constant at -0.51 m/s² resulting in a near-linear increase and decrease of wheel velocity; thus, bringing the robot to a stable stop while the wheels maintain contact with the ground at all times since the pitch angle varies between ± 1.2 deg.

In a separate experiment, the $M_{ext} = 1$ kg case scenario was repeated while the robot ascended a 10 deg incline in the controlled mode as shown in Fig. 11. Control actions are once again observable in fluctuations of the robot acceleration (Fig. 11(a)). After 2.5 s the algorithm limits the robot acceleration within the maximum allowable acceleration region of ± 0.2 m/s² (Fig. 7). From Fig. 11(b), the maximum wheel velocity peaks at 390 rpm as opposed to 2500 rpm on flat terrain in the controlled mode (Fig. 10(b)). The control algorithm prevents the robot from tipping over in both the acceleration and deceleration phases.

For the $M_{ext} = 2.5$ kg case scenario on flat terrain, shown in Fig. 12, the robot was only operated in the controlled mode to prevent the robot from damage if tipped over. The algorithm successfully limited the robot acceleration (Fig. 12(a)) to the maximum allowable range of ± 0.5 m/s² (obtained from Fig. 7) after 2.4 s that maintained the robots stability and prevented tipping over. From Fig. 12(b), it can be noted that the maximum wheel velocity peaks at 330 rpm. During the acceleration phase, although the robot did reach a maximum acceleration of 2 m/s², the time span of this large acceleration was 0.16 s, too short to cause the robot to lose stability.

4.3 Multi-Directional Mobility. As mentioned in Sec. 1, the reconfiguration procedure of modular robots will benefit from multi-directional mobility due to the enhanced spatial alignment capabilities with respect to a docking target. Using the proposed multi-directional robot, a docking procedure is performed as depicted in Fig. 13. In this experiment the proposed robot and docking target are fitted with coupling mechanisms [19,20] that

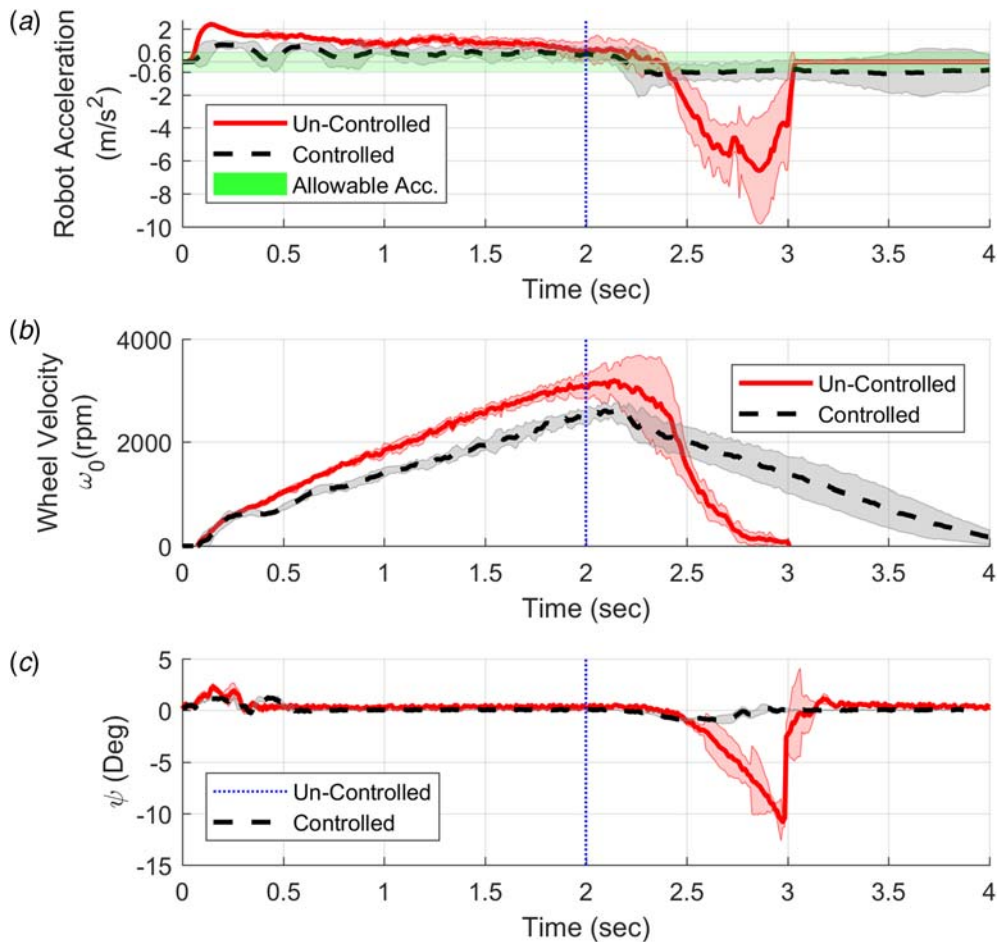


Fig. 10 Experimental results of an attached external payload $M_{ext} = 1$ kg case scenario: (a) robot acceleration, (b) wheel velocity, and (c) robot pitch angle ψ

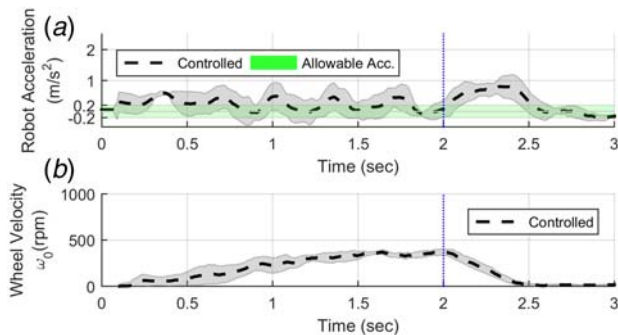


Fig. 11 Experimental results of an attached external payload $M_{ext} = 1$ kg while robot ascends a 10 deg inclined plane: (a) robot acceleration and (b) wheel velocity

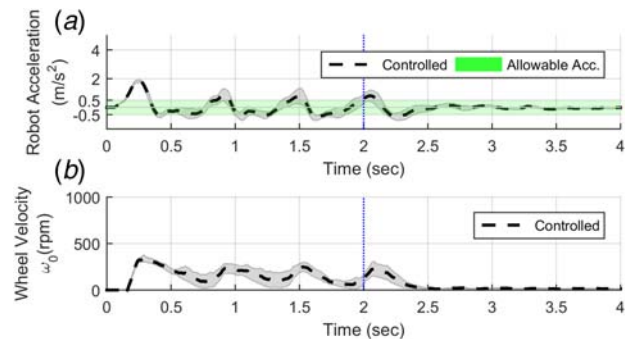


Fig. 12 Dynamic stability experimental results of an attached external payload $M_{ext} = 2.5$ kg case scenario: (a) robot acceleration and (b) wheel velocity

must be aligned to enable successful docking. The aim of this experiment is to demonstrate the benefits of multi-directional mobility and its implications to the field of modular reconfigurable robotics [39].

The proposed robot is initially misaligned from the docking target with respect to the global coordinate frame $X'Y'Z'$ by values $\{50, 50, 5\}$ cm and $\{0, 0, 90\}$ deg. The robot first translates longitudinally using its WU along the $-X'$ -axis, Fig. 13(a). The VTU is then used to provide translational vertical mobility along the Z' -axis, Fig. 13(b). Once in the wheeled mode, the WUs are used to provide translational lateral mobility along the Y' -axis, Fig. 13(c), then rotational yaw mobility about the Z' -axis, Fig. 13(d). Finally,

the robot translates laterally along the $-X'$ -axis, Fig. 13(e), and can successfully dock with its target, Fig. 13(f). Although the robot cannot produce mobility in the roll or pitch directions, misalignments along these directions can be tolerated using the coupling mechanisms active roll joint and specially designed clamping profiles [19,20], respectively.

5 Conclusion

This paper presented the design, analysis, and experimental results of a novel mobile robot with multi-directional mobility that utilizes a hybrid combination of tracks and wheels that

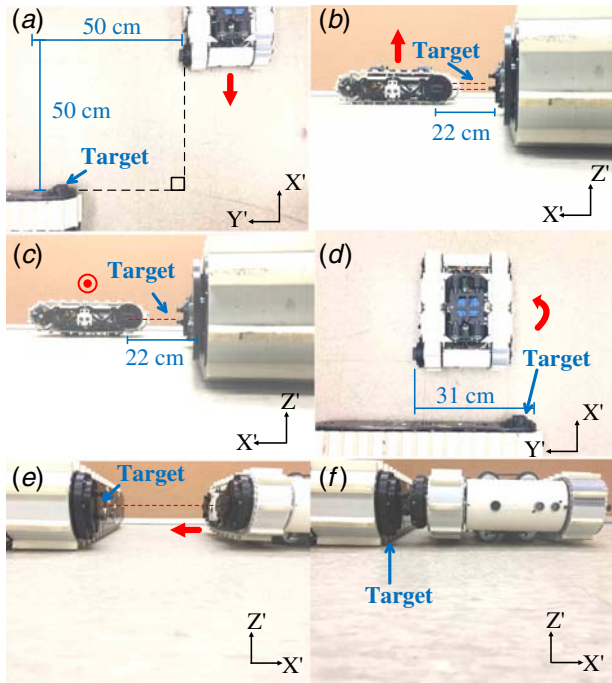


Fig. 13 Benefits of multi-directional mobility during a reconfiguration procedure: (a) translational longitudinal mobility along the $-X'$ -axis, (b) translational vertical mobility along the Z' -axis, (c) translational lateral mobility along the Y' -axis, (d) yaw mobility along the Z' -axis, (e) translational lateral mobility along the $-X'$ -axis, and (f) successful docking

provide two modes of locomotion in the longitudinal and lateral direction, respectively. A vertical translation mechanism provides an additional axis of mobility that can adjust the height of the mobile robot by elevating the tracks above the ground. Furthermore, the robot can rotate in the yaw direction during both locomotion modes via differential drive. The robot measures $410 \times 305 \times 120$ mm to maintain an aspect ratio of ~ 1 – 1.8 for effective turning during tracked locomotion [40], weighs 9 kg and can produce a forward velocity of 2.65 and 3.55 m/s in tracked and wheeled locomotion modes, respectively. To stabilize the robot during wheeled locomotion, a dynamic stability algorithm had been developed and verified experimentally while carrying various external payloads.

5.1 Broader Impact. The results of this research have a broader impact for applications spanning multiple fields in mobile robotics. The enhanced features of a multi-directional mobility platform can enable precise spatial alignment between modular robots in order to overcome translational and rotational misalignments and increase the probability of successful docking during reconfiguration procedures [21], as demonstrated experimentally in Sec. 4.3. Furthermore, this research addresses the need of multi-directional, adaptive mobility that can maintain dynamic stability and carry heavy payloads that can provide a useful solution in industrial mobile robotics for autonomous pick and place applications [41], as demonstrated experimentally in Sec. 4.2. Such benefits of hybrid locomotion provide the additional benefit of switching between wheeled and tracked locomotion to adapt to various terrain types, which can prove useful to the field of assistive mobility systems such as intelligent robotic wheel chairs for the handicapped [42], as demonstrated experimentally in Sec. 4.1.

Acknowledgment

The authors would like to thank Shumin Feng and Prashant Kumar for their assistance in prototype integration and experimental data collection.

Nomenclature

- b_{ext} = distance $\overline{C_W C_{ext}}$ along the X -axis
- h_W = location of C_W relative to the ground along the Y -axis
- z_{VTM} = distance between the bottom track segments and the ground along the Y -axis, also defined as the displacement of the VTM relative to the ground
- C_{ext} = center of mass of external payload
- C_W = center of mass of the combined wheeled units and the VTM assembly
- $\hat{i}\hat{j}\hat{k}$ = unit vectors of the XYZ Cartesian frame, respectively
- b_L, b_R = distance $\overline{C_W C_L}$ and $\overline{C_W C_R}$ along the X -axis, respectively
- b_{P_L}, b_{P_R} = distance $\overline{C_W P_L}$ and $\overline{C_W P_R}$ along the X -axis, respectively
- $h_{L_0}, h_{R_0}, h_{ext}$ = location of C_L, C_R and C_{ext} relative to the bottom track segments along the Y -axis, respectively
- C_L, C_R = respective center of mass of left- and right-tracked units
- M_L, M_R, M_W, M_{ext} = mass of left-tracked unit, right-tracked unit, wheeled unit, and external load, respectively
- P_L, P_R = contact point (surface) between the ground and the left and right wheels of the wheeled unit, respectively
- α, ψ = ground inclination and robot pitch angle (or tilt) around the Z -axis, respectively

References

- [1] Moore, K. L., and Flann, N. S., 2000, "A Six-Wheeled Omnidirectional Autonomous Mobile Robot," *IEEE Cont. Syst. Mag.*, **20**(6), pp. 53–66.
- [2] Bayar, G., Koku, A. B., and ilhan Konukseven, E., 2009, "Design of a Configurable all Terrain Mobile Robot Platform," *Dimensions*, 2000(225 \times 400x), p. 225 \times 400x.
- [3] Bayar, G., Koku, A. B., and ilhan Konukseven, E., 2009, "Design of a Configurable all Terrain Mobile Robot Platform," *Int. J. Math. Models Methods Appl. Sci.*, **3**(4), pp. 366–373.
- [4] Michaud, F., Letourneau, D., Arsenault, M., Bergeron, Y., Cadrin, R., Gagnon, F., Legault, M. A., Millette, M., Paré, J. F., Tremblay, M. C., and Lepage, P., 2005, "Multi-Modal Locomotion Robotic Platform Using Leg-Track-Wheel Articulations," *Auton. Rob.*, **18**(2), pp. 137–156.
- [5] Li, Z., Ma, S., Li, B., Wang, M., and Wang, Y., 2009, "Parameter Design and Optimization for Mobile Mechanism of a Transformable Wheel-Track Robot," 2009 IEEE International Conference on Automation and Logistics, Shenyang, China, Aug. 5–7, pp. 158–163.
- [6] Lee, J. W., Kim, B. S., and Song, J. B., 2009, "A Small Robot Based on Hybrid Wheel-Track Mechanism," *Trans. Korean Soc. Mech. Eng. A*, **33**(6), pp. 545–551.
- [7] Kim, J., Kim, Y.G., Kwak, J.H., Hong, D.H., and An, J., 2010, "Wheel & Track Hybrid Robot Platform for Optimal Navigation in an Urban Environment," Proceedings of SICE Annual Conference, Taipei, Taiwan, Aug. 18–21, pp. 881–884.
- [8] Root, M. "Next-Generation Unmanned Ground Vehicle is Lighter, Faster, Stronger and More Intelligent," <http://news.northropgrumman.com/news/releases/photo-release-northrop-grumman-remotec-to-begin-delivering-titus-robot-in-december>. Accessed December 13, 2017
- [9] Shen, S.Y., Li, C.H., Cheng, C.C., Lu, J.C., Wang, S.F., and Lin, P.C., 2009, "Design of a Leg-Wheel Hybrid Mobile Platform," 2009 IEEE/RSJ International Conference on Intelligent Robots and Systems, St. Louis, MO, Oct. 10–15, pp. 4682–4687.
- [10] Mutka, A., and Kovacic, Z., 2011, "A Leg-Wheel Robot-Based Approach to the Solution of Flipper-Track Robot Kinematics," 2011 IEEE International Conference on Control Applications (CCA), Denver, CO, USA, Sept. 28–30, pp. 1443–1450.
- [11] Michaud, F., Letourneau, D., Arsenault, M., Bergeron, Y., Cadrin, R., Gagnon, F., Legault, M.A., Millette, M., Pare, J.F., Tremblay, M.C., and Lepage, P., 2003, "AZIMUT, a Leg-Track-Wheel Robot," Proceedings 2003 IEEE/RSJ International Conference on Intelligent Robots and Systems (IROS 2003) (Cat. No. 03CH37453), Vol. 3, Las Vegas, NV, Oct. 27–31, pp. 2553–2558.
- [12] Kwon, H.J., Shim, H., Kim, D.G., Park, S.K., and Lee, J., 2007, "A Development of a Transformable Caterpillar Equipped Mobile Robot," 2007 International Conference on Control, Automation and Systems, Seoul, South Korea, Oct. 17–20, pp. 1062–1065.
- [13] Gao, X., Cui, D., Guo, W., Mu, Y., and Li, B., 2017, "Dynamics and Stability Analysis on Stairs Climbing of Wheel-Track Mobile Robot," *Int. J. Adv. Rob. Syst.*, **14**(4), pp. 1–13. .

- [14] Ian, R., 2017, "Stairclimbing Wheelchairs: Fact and Fiction," <https://www.youtube.com/watch?v=AZ9DotVwhlQ>. Accessed May 1, 2018.
- [15] Salih, J. E. M., Rizon, M., Yaacob, S., Adom, A. H., and Mamat, M. R., 2006, "Designing Omni-Directional Mobile Robot with Mecanum Wheel," *Am. J. Appl. Sci.*, **3**(5), pp. 1831–1835.
- [16] Udengaard, M., and Iagnemma, K., 2009, "Analysis, Design, and Control of an Omnidirectional Mobile Robot in Rough Terrain," *ASME J. Mech. Des.*, **131**(12), pp. 121002.
- [17] Kumar, P., Saab, W., and Ben-Tzvi, P., 2017, "Design of a Multi-Directional Hybrid-Locomotion Modular Robot With Feedforward Stability Control," ASME 2017 International Design Engineering Technical Conferences and Computers and Information in Engineering Conference, Cleveland, OH, Aug. 6–9, ASME no. V05BT08A010.
- [18] Ben-Tzvi, P., and Moubarak, P.M., 2015, "Mobile Robot With Hybrid Traction and Mobility Mechanism," U.S. Patent 9,004,200.
- [19] Saab, W., and Ben-Tzvi, P., 2015, "Development of a Novel Coupling Mechanism for Modular Self-Reconfigurable Mobile Robots," ASME 2015 International Design Engineering Technical Conferences and Computers and Information in Engineering Conference, Boston, MA, Aug. 2–5, ASME no. V05BT08A007.
- [20] Saab, W., and Ben-Tzvi, P., 2016, "A Genderless Coupling Mechanism With Six-Degrees-of-Freedom Misalignment Capability for Modular Self-Reconfigurable Robots," *ASME J. Mech. Rob.*, **8**(6), p. 061014.
- [21] Ben-Tzvi, P., 2017, "STORM: Self-Configurable and Transformable Omnidirectional Robotic Modules," <https://youtu.be/1Y7wd6yHATY>. Accessed May 1, 2018.
- [22] Arvin, F., Samsudin, K., and Nasser, M. A., 2009, "Design of a Differential-Drive Wheeled Robot Controller With Pulse-Width Modulation," 2009 Innovative Technologies in Intelligent Systems and Industrial Applications, Monash, Malaysia, July 25–26, pp. 143–147.
- [23] Gysen, B. L., Paulides, J. J., Janssen, J. L., and Lomonova, E. A., 2010, "Active Electromagnetic Suspension System for Improved Vehicle Dynamics," *IEEE Trans. Vehicular Technol.*, **59**(3), pp. 1156–1163.
- [24] Gysen, B. L., Janssen, J. L., Paulides, J. J., and Lomonova, E. A., 2009, "Design Aspects of an Active Electromagnetic Suspension System for Automotive Applications," *IEEE Trans. Ind. Appl.*, **45**(5), pp. 1589–1597.
- [25] Sankaranarayanan, V., Emekli, M. E., Gilvenc, B. A., Guvenc, L., Ozturk, E. S., Ersolmaz, E. S., Eyol, I. E., and Sinal, M., 2008, "Semiactive Suspension Control of a Light Commercial Vehicle," *IEEE/ASME Trans. Mechatron.*, **5**(13), pp. 598–604.
- [26] Waldron, K. J., and Abdallah, M. E., 2007, "An Optimal Traction Control Scheme for Off-Road Operation of Robotic Vehicles," *IEEE/ASME Trans. Mechatron.*, **12**(2), pp. 126–133.
- [27] Amodeo, M., Ferrara, A., Terzaghi, R., and Vecchio, C., 2010, "Wheel Slip Control via Second-Order Sliding-Mode Generation," *IEEE Trans. Intell. Transp. Syst.*, **11**(1), pp. 122–131.
- [28] Imine, H., Fridman, L. M., and Madani, T., 2012, "Steering Control for Rollover Avoidance of Heavy Vehicles," *IEEE Trans. Vehicular Technol.*, **61**(8), pp. 3499–3509.
- [29] Messuri, D., and Klein, C., 1985, "Automatic Body Regulation for Maintaining Stability of a Legged Vehicle During Rough-Terrain Locomotion," *IEEE J. Rob. Autom.*, **1**(3), pp. 132–141.
- [30] Ghasempoor, A., and Sepehri, N., 1995, "A Measure of Machine Stability for Moving Base Manipulators," Proceedings of 1995 IEEE International Conference on Robotics and Automation, Vol. 3, Nagoya, Japan, May 21–27, pp. 2249–2254.
- [31] Yuk, G. H., Cho, W. H., and Yang, H. S., 2012, "Practical Implementation of the Normalized Dynamic Energy Stability Margin for Wheeled Robots," *Int. J. Precision Eng. Manuf.*, **13**(1), pp. 49–56.
- [32] McGhee, R. B., and Frank, A. A., 1968, "On the Stability Properties of Quadruped Creeping Gaits," *Math. Biosci.*, **3**, pp. 331–351.
- [33] Song, S. M., and Waldron, K. J., 1989, *Machines That Walk: The Adaptive Suspension Vehicle*, MIT press, MA.
- [34] Sugano, S., Huang, Q., and Kato, I., 1993, "Stability Criteria in Controlling Mobile Robotic Systems," Proceedings of 1993 IEEE/RSJ International Conference on Intelligent Robots and Systems (IROS'93), Vol. 2, Yokohama, Japan, July 26–30, pp. 832–838.
- [35] Vukobratović, M., and Borovac, B., 2004, "Zero-moment Point—Thirty Five Years of its Life," *Int. J. Humanoid Rob.*, **1**(01), pp. 157–173.
- [36] Kim, J., Chung, W. K., Youm, Y., and Lee, B. H., 2002, "Real-Time ZMP Compensation Method Using Null Motion for Mobile Manipulators," Proceedings 2002 IEEE International Conference on Robotics and Automation (Cat. No. 02CH37292), Vol. 2, Washington, DC, May 11–15, pp. 1967–1972.
- [37] Papadopoulos, E. G., and Rey, D. A., 1996, "A New Measure of Tipover Stability Margin for Mobile Manipulators," Proceedings of IEEE International Conference on Robotics and Automation, Vol. 4, Minneapolis, MN, Apr. 22–28, pp. 3111–3116.
- [38] Dube, C., 2013, "Experimental Validation of Tip Over Stability of a Tracked Mobile Manipulator," 2013 Africon, Pointe-Aux-Piments, Mauritius, Sept. 9–12, pp. 1–6.
- [39] Moubarak, P., and Ben-Tzvi, P., 2012, "Modular and Reconfigurable Mobile Robotics," *Rob. Auton. Syst.*, **60**(12), pp. 1648–1663.
- [40] Schempf, H., 1995, "Houdini: Site and Locomotion Analysis-Driven Design of an In-Tank Mobile Cleanup Robot," American Nuclear Society Winter Meeting Transactions, (CONF-951006-41).
- [41] Guizzo, E., 2008, "Three Engineers, Hundreds of Robots, One Warehouse," *IEEE Spectr.*, **45**(7), pp. 26–34.
- [42] Gomi, T., and Griffith, A., 1998, "Developing Intelligent Wheelchairs for the Handicapped," Assistive Technology and Artificial Intelligence. Lecture Notes in Computer Science, vol 1458, V. O. Mittal, H. A. Yanco, J. Aronis and R. Simpson, eds., Springer, Berlin, Heidelberg, pp. 150–178.